Int. J. Heat Mass Transfer. Vol. 33, No. 6, pp. 1149–1163, 1990
Printed in Great Britain

0017–9310/90 $3.00 + 0.00

Numerical study of steady state and transient laser melting problems—I. Characteristics of flow field and heat transfer

BISWAJIT BASU
Tata Research Development and Design Centre, 1, Mangaldas Road, Pune 411 001, India

and

A. W. DATE
Department of Mechanical Engineering, Indian Institute of Technology, Powai, Bombay 400 076, India

(*Received* 6 *September* 1988 *and in final form* 30 *January* 1989)

Abstract—Steady state and transient laser melting problems are numerically simulated. Enthalpy formulation is used for solving the energy equation and momentum equations are solved only in the liquid domain by the SIMPLE algorithm. Using a Gaussian distribution of input heat flux, a wide range of studies are performed for steel and aluminium by varying the beam power density and the beam radius. The pool shape and the surface tension driven flow field are found to be quite different in nature for steel and aluminium. The streamline plots show the existence of two contra-rotating cells in the molten pool the size and strength of which are found to be strongly dependent on the material property, i.e. the Prandtl number.

1. INTRODUCTION

THE STUDY of laser–material interaction has been one of the important fields of research recently. Laser surface treatments are capable of producing new properties and new materials due to the associated rapid heating and cooling rates which are of the order of millions of degrees per second. Improved properties like greater resistance to wear and corrosion can be produced through laser surface treatment. New materials (e.g. quasi crystals) have been developed using laser surface heating.

It has been pointed out by many researchers [1–5] that fluid flow plays an important role during laser melting and solidification. Mehrabian *et al.* [1] reported the relationship between microstructure and fluid flow pattern with an aluminium–copper alloy under laser melting and solidification with a beam density of 10^{10} W m^{-2}. From the study of microstructure, they observed a circular convection pattern just below the melt. Structural analysis revealed that vigorous convection occurred in the middle of the melt.

Anthony and Cline [2] carried out the first quantitative analysis and proposed that the flow in the molten pool is created by the surface tension gradient. Srinivasan and Basu [3] have recently shown the negligible effect of the buoyancy force in the laser melted pool. Anthony and Cline [2], however, presented a one-dimensional study and, as a result, the flow field is not coupled to the heat transfer.

Chan *et al.* [4] proposed the first numerical model of transient laser melting with fluid flow. Unfortunately they neglected the solid/liquid interface energy balance since wrong values of latent heat of fusion were employed. Their analysis is thus based on an assumption which is not physically correct. However, they presented quantitative effects of different process parameters, such as beam power density, radius and material, on the pool shape, surface temperature and cooling rate. In their subsequent work, Chan *et al.* [5] analysed the steady state laser melting problem within the power range of 10^7–10^9 W m^{-2}. They found that the scanning velocity plays an insignificant role because of the higher magnitude of the surface tension velocity. Later, this fact was also proved by Srinivasan and Basu [3]. Chan *et al.* [6] analysed laser melting at different cross-sections along the laser scan direction. Recently, Basu and Srinivasan [7] presented a detailed analysis of the flow pattern in the laser melted pool through a steady state analysis. They assumed a top-hat heat flux distribution and used the vorticity–stream function method for solving the momentum equation in the molten region. They have shown that the flow pattern is characterized by the existence of two contra-rotating cells. The effect of these cells on the total heat transfer is presented and the role of secondary cells in controlling the pool shape is analysed.

In all the previous studies [4–7], the effect of beam power, beam radius and material on the flow field and heat transfer have not been studied. Moreover, transient flow development during laser melting has not yet been reported.

NOMENCLATURE

a	finite difference coefficients
B_f	boundary heating factor, $q''r_0C_{pl}/k_l\lambda$
C	convective coefficient
C_p	specific heat [J kg^{-1} K^{-1}]
d	diffusion coefficient
H	enthalpy [J kg^{-1}]
H_s	enthalpy of saturated solid [J kg^{-1}]
ΔH	non-dimensional latent heat content
K	thermal conductivity [W m^{-1} K^{-1}]
Ma	Marangoni number, U_Rr_0/α
p	pressure [N m^{-2}]
Pr	Prandtl number, ν/α
Q	heat flux
q''	power density of the beam [W m^{-2}]
r	radial coordinate [m]
r_0	radius of the beam [m]
r_{max}	maximum width of the molten pool
R	residue of the finite difference equation
R_σ	surface tension Reynolds number, U_Rr_0/ν
Ste	Stefan number, $C_p(T_m-T_\infty)/\lambda$
T	temperature [K]
t	time [s]
U	surface tension reference velocity, $((d\sigma/dT)\cdot\lambda)/(C_{pl}\cdot\mu)$
v_r	radial velocity [m s^{-1}]
v_z	axial velocity [m s^{-1}]
z	axial coordinate [m].

Greek symbols

α	thermal diffusivity [m^2 s^{-1}]
ε, γ	convergence criterion
θ	non-dimensional temperature
λ	latent heat of fusion [J kg^{-1}]
μ	dynamic viscosity [kg m^{-1} s^{-1}]
ν	kinematic viscosity [m^2 s^{-1}]
ρ	density [kg m^{-3}]
τ	non-dimensional time
ϕ	non-dimensional enthalpy
ψ	non-dimensional stream function
Ω	non-dimensional vorticity.

Subscripts

l	liquid
m	melting point
nb	neighbouring points
P	control volume under computation
s	solid
∞	ambient.

Superscripts

*	dimensional value
n	new time level
o	old time level.

In this paper, a detailed steady state analysis of flow field and heat transfer is presented under varying beam characteristics and materials. The flow development in the molten pool is studied through transient analysis. The study is performed using momentum equations in primitive variables that are solved by the SIMPLE algorithm.

2. DEFINITION OF THE PROBLEM

The problem is physically defined as follows (see Fig. 1).

A laser beam of constant power with Gaussian heat flux distribution strikes the surface of an opaque material. All of the incident radiation is assumed to be absorbed by the material. The heat absorbed develops a molten pool. The flow in the molten pool is produced due to the surface tension gradient. The latter is produced as a result of the surface temperature gradient. The surface tension gradient acts as a shear stress at the free surface and, in turn, drives the flow. The problem is to determine the flow pattern, isotherms and isobars in the melt, the pool shape and the free surface velocity field and the temperature distributions at the free surface under varying beam characteristics and for different materials at steady state. The flow development is also studied to analyse the formation and interactions between the contra-rotating cells in the molten pool.

The following assumptions are made for the present model.

(1) The heat conduction and fluid flow are primarily in the r and z directions. Conduction and convection in the angular direction are neglected due to the symmetry.

(2) All the properties of the material except the surface tension are independent of temperature.

(3) The free surface of the melt is flat [7].

(4) The laser beam is stationary [3, 5].

(5) The flow in the melt is laminar. The conditions for onset of turbulence for surface tension driven flow in the cavity are not known and hence the flow is assumed to be laminar.

(6) The buoyancy force is of negligible order of magnitude [3].

(7) The top surface outside the beam is adiabatic.

(8) The heat flux at the boundary represents the net heat input to the material.

It may be noted that assumptions 3 and 8 may have to be revised in future as surface rippling phenomena have been observed in laser applications [2] and materials can have emissivity of less than unity [8].

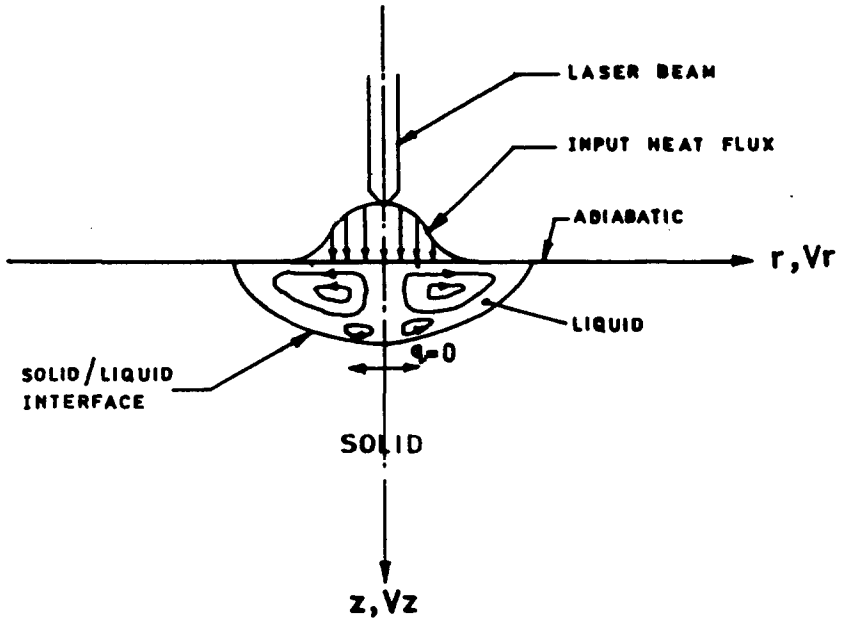

FIG. 1. Physical problem of laser melting along with the geometry.

3. MATHEMATICAL FORMULATION

The two-dimensional transient equations of momentum and energy transport and continuity in the r–z plane, when non-dimensionalized with the following variables, i.e.

$$\mathrm{r} = \frac{\mathrm{r}^*}{r_0}; \quad \mathrm{v} = \frac{\mathrm{v}^*}{U_R}; \quad p = \frac{p^*}{\rho U_R^2}; \quad \theta = \frac{C_p(T-T_m)}{\lambda};$$

$$\phi = \frac{H-H_s}{\lambda}; \quad \tau = \frac{t\alpha_l}{r_0^2}; \quad k = \frac{k^*}{k_l^*}; \quad U_R = \frac{\frac{d\sigma}{dT}\cdot\lambda}{C_{pl}\cdot\mu};$$

$$R_\sigma = \frac{U_R r_0}{\nu}; \quad Ma = \frac{U_R r_0}{\alpha_l}; \quad B_f = \frac{q'' r_0 C_{pl}}{k_l \lambda}$$

$$\text{and} \quad Ste = \frac{C_{ps}(T_m - T_\infty)}{\lambda}$$

yield the following set of coupled equations:

energy equation

$$\frac{\partial\phi}{\partial\tau} + Ma\left[\frac{1}{r}\frac{\partial}{\partial r}(rv_r\phi) + \frac{\partial}{\partial z}(v_z\phi)\right] = \frac{1}{r}\frac{\partial}{\partial r}\left(kr\frac{\partial\theta}{\partial r}\right) + \frac{\partial}{\partial z}\left(k\frac{\partial\theta}{\partial z}\right); \quad (1)$$

r-momentum equation

$$\frac{1}{Ma}\frac{\partial v_r}{\partial\tau} + \frac{1}{r}\frac{\partial}{\partial r}(rv_r^2) + \frac{\partial}{\partial z}(v_r v_z) = -\frac{\partial p}{\partial r} + \frac{1}{R_\sigma}\left[\frac{\partial}{\partial r}\left\{\frac{1}{r}\frac{\partial}{\partial r}(rv_r)\right\} + \frac{\partial}{\partial z}\left(\frac{\partial v_r}{\partial z}\right)\right]; \quad (2)$$

z-momentum equation

$$\frac{1}{Ma}\frac{\partial v_z}{\partial\tau} + \frac{1}{r}\frac{\partial}{\partial r}(rv_r v_z) + \frac{\partial}{\partial z}(v_z^2) = -\frac{\partial p}{\partial z} + \frac{1}{R_\sigma}\left[\frac{1}{r}\frac{\partial}{\partial r}\left(r\frac{\partial v_z}{\partial r}\right) + \frac{\partial}{\partial z}\left(\frac{\partial v_z}{\partial z}\right)\right]; \quad (3)$$

continuity equation

$$\frac{1}{r}\frac{\partial}{\partial r}(rv_r) + \frac{\partial v_z}{\partial z} = 0. \quad (4)$$

The corresponding boundary conditions are as follows:

$$\text{at } r = 0; \quad \frac{\partial\theta}{\partial r} = \frac{\partial v_z}{\partial r} = v_r = 0; \quad 0 \leqslant z \leqslant D \quad (5)$$

$$\text{at } r = w; \quad \theta = -Ste; \quad 0 \leqslant z \leqslant D \quad (6)$$

$$\text{at } z = 0; \quad \theta = -Ste; \quad 0 \leqslant r \leqslant W \quad (7)$$

at $z = D$;

$$\left.\begin{aligned} -\frac{\partial\theta}{\partial z} &= B_f \exp(-2r^2); & 0 \leqslant r \leqslant 1 \\ &= 0; & 1 \leqslant r \leqslant W \\ -\frac{\partial v_r}{\partial z} &= \frac{\partial\theta}{\partial r}, \; v_z = 0; & 0 \leqslant r \leqslant r_{max} \end{aligned}\right\}. \quad (8)$$

The pool shape, the flow and temperature distributions are thus governed by B_f, Pr, R_σ and Ste. As such, the equations are solved for given input values of B_f, Ste, Pr and R (or $Ma = R_\sigma \cdot Pr$). The selected values of D and W used for computation, which represent infinity as shown in Fig. 1, are 6.5 and 6.0,

respectively, after comparing with the results of higher computational domain, i.e. $D = 7.5$ and $W = 7.0$. After obtaining the converged solution (both steady state and transient), the stream function distribution is extracted from v_r and v_z via the stream function equation which is of the following form:

$$\frac{\partial}{\partial z}\left(\frac{1}{r}\frac{\partial \psi}{\partial z}\right)+\frac{\partial}{\partial r}\left(\frac{1}{r}\frac{\partial \psi}{\partial r}\right)+r\Omega = 0 \qquad (9)$$

where

$$\Omega = \frac{1}{r}\frac{\partial v_r}{\partial z}-\frac{1}{r}\frac{\partial v_z}{\partial z}. \qquad (10)$$

The stream function has a constant value (say zero) along all boundaries.

4. NUMERICAL DETAILS

Following the notation of Patankar [9], the finite difference equations of the energy and momentum equations are as follows:

energy

$$a_P^o\phi_P^n + a_P\theta_P^n = \sum d_{nb}\theta_{nb}^n + \sum C_{nb}\phi_{nb}^n + \text{Source}$$

where

$$a_P^o = \sum C_{nb} + \frac{r_P\Delta r_P\Delta z_P}{\Delta\tau}; \quad a_P = \sum d_{nb}; \qquad (11)$$

momentum

$$(a_P^o + a_P)v_P^n = \sum (d_{nb}+C_{nb})v_{nb}^n + \text{Source} \qquad (12)$$

where

$$a_P^o = \frac{r_P\Delta r_P\Delta z_P}{Ma\cdot\Delta\tau}; \quad a_P = \sum (d_{nb}+C_{nb}).$$

In equations (11) and (12), a, d and C are coefficients that affect diffusion (i.e. d) and convection (i.e. C).

The momentum equations, along with the continuity equation, are solved by the SIMPLE algorithm [9] in the staggered grid arrangement. The finite difference equations are solved by the Gauss–Seidal method. The energy equation is also solved by the Gauss–Seidal method, maintaining the proper enthalpy and temperature relationships. The following generalized (θ–ϕ) relationship [10], which is valid in all three regions, i.e. solid, phase change and liquid, is used during computation:

$$\theta = \left(\frac{\phi-|\phi|}{2}\right)+\left(\frac{\phi-1+|1-\phi|}{2}\right). \qquad (13)$$

4.1. *Grids*

The steady state results are obtained with 26×26 grids, whereas 38×38 grids are used to study the transient flow development. Variable grids are used with very fine grids under the beam where high temperature gradients exist. A typical grid distribution is shown in Fig. 2.

4.2. *Treatment of solid/liquid boundary*

Momentum equations are solved in the liquid control volumes only. The velocity in the two phase control volume, i.e. the control volume that contains the interface, is assumed to be of negligible order of magnitude. The liquid control volumes are identified on the basis of the latent heat content. Let ΔH_P^l represent the latent heat content of a control volume, then the velocity components of this control volume are set to zero, if

$$\Delta H_P^l < \lambda.$$

ΔH_P^l is calculated in the following way:

$$\text{for } v_r, \quad \Delta H_P^l = \frac{(\Delta H_{P,P}^l + \Delta H_{P,E}^l)}{2.0}$$

$$\text{for } v_z, \quad \Delta H_P^l = \frac{(\Delta H_{P,P}^l + \Delta H_{P,N}^l)}{2.0}$$

where suffices E and N represent control volumes to the east and north of P, respectively.

Once the liquid control volumes are identified on the basis of the latent heat content (ΔH_P^l), the pressure correction boundary condition is applied in the following manner.

If $\Delta H_{P,P}^l \geq \lambda$ and $\Delta H_{P,E}^l < \lambda$; $d_E^{P'} = 0.0$.

If $\Delta H_{P,P}^l \geq \lambda$ and $\Delta H_{P,W}^l < \lambda$; $d_W^{P'} = 0.0$.

If $\Delta H_{P,P}^l \geq \lambda$ and $\Delta H_{P,N}^l < \lambda$; $d_N^{P'} = 0.0$.

If $\Delta H_{P,P}^l \geq \lambda$ and $\Delta H_{P,S}^l < \lambda$; $d_S^{P'} = 0.0$.

The solution of the momentum equation is therefore based on an approximated solid/liquid interface and this is shown in Fig. 2.

4.3. *Convergence criteria*

Convergence of both steady state and transient solutions is checked based on the following criteria.

(i) *Fractional change criterion.*

$$\left|\frac{W_P^{n+1}-W_P^n}{W_P^n}\right| \leq \varepsilon; \quad \varepsilon = 10^{-3}$$

where W is any variable; v_r, v_z, ϕ and 'n' is the iteration level for both the steady state and transient solutions.

(ii) *Residual error criterion.* For momentum equations the residue error, R_P, of the finite difference equations is checked as follows:

$$|R_P|_{max} \leq \varepsilon; \quad \varepsilon = 10^{-7}$$

where R_P is given as

$$R_P = \sum (d_{nb}+C_{nb})v_{nb}^n - (a_P^o + a_P)v_P^n + \text{Source}.$$

For the energy equation, the 'global residual norm' is minimized and the criterion for checking is defined as follows [11]:

$$\frac{\|R\|^m}{\|R\|^o} \leq \gamma \quad \gamma = 0.05 \text{ for steady state equation}$$

$$= 0.2 \text{ for transient equation}$$

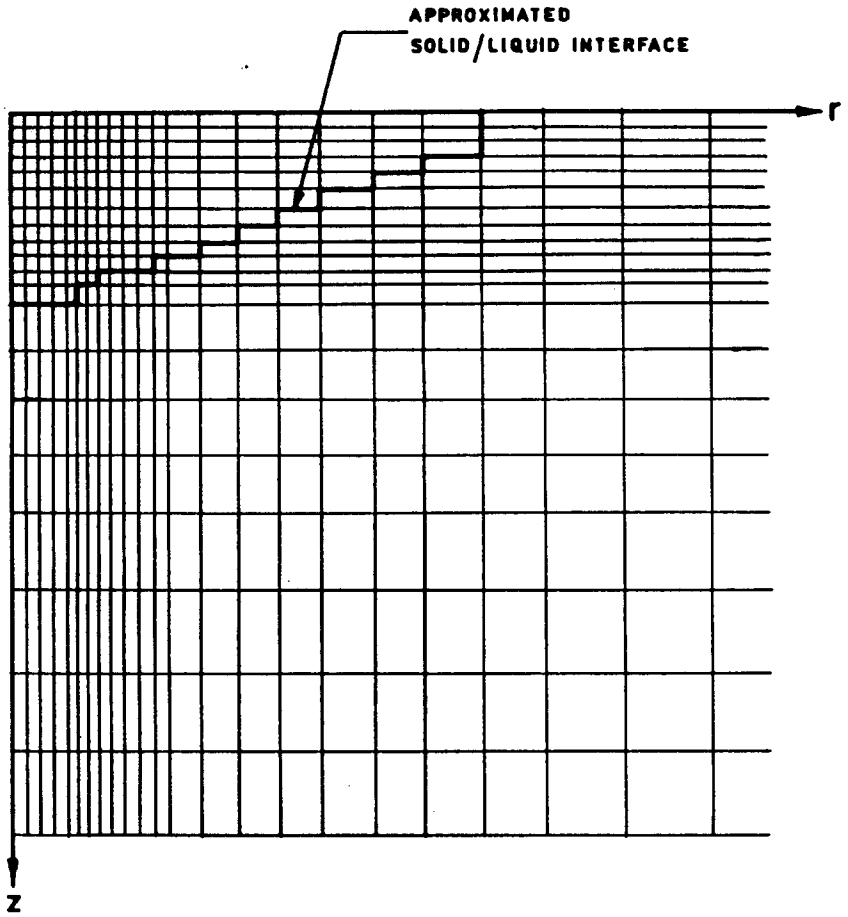

FIG. 2. Non-uniform grid distribution used for computation along with the approximation of interface.

where $\|R\|$, the Euclidean norm of the residues, is defined as

$$\|R\| = \left[\sum_{\text{for all } P} (R_P)^2\right]^{1/2}.$$

o and m represent the first iteration and current iteration levels, respectively.

For steady state calculations, the overall heat balance criterion is also used to check the convergence. This criterion is defined as follows:

$$\left[\frac{Q_{\text{in}} - Q_{\text{out|interface}}}{Q_{\text{out|interface}}}\right] \leqslant \varepsilon; \quad \varepsilon = 0.01.$$

For steady state runs, the converged solution is first obtained for the beam of lower power and this solution is subsequently used as the guessed solution for the beams of higher power. This methodology is followed to save computer time. For a typical steady state run for low power cases, the CPU time is around 20 min on the ELXSI 6400 system. The number of iterations is around 3500 with the following relaxation parameters that were found to be necessary:

$$\omega_{\text{energy}} = \omega_{\text{momentum}} = 0.4 \quad \text{and} \quad \omega_{\text{Pr. corr}} = 0.6.$$

5. RESULTS AND DISCUSSION

5.1. *Validation of the computer code*

In order to validate the computer code, an experiment reported by Sekhar [12] has been simulated. The experiment was carried out on a 10 kW electron beam machine. The beam diameter is 1.0 mm and the material is Al–4.5% Cu. The heat flux profile is top-hat. The melt depth and width were measured after solidification through the micrographs. During numerical simulation, the electromagnetic force is neglected and thereby the flow is assumed to be driven by surface tension only. This assumption is based on the paper of Kou and Sun [13] where they have shown that the velocity field with a surface tension gradient during electron beam welding is always one order higher than that with electromagnetic force.

Table 1 shows the non-dimensional parameters for the numerical simulation. Table 2 shows the experimental and numerical melt depths and widths under various conditions. It can be seen that numerical and experimental results are in good agreement except for the case of the lowest beam power. The reason for this deviation may be due to the error in measuring pool depths and widths of very small dimensions. Elec-

Table 1. Property values of Al–4.5% Cu and process parameters

T_m	$= 821.0$ K
λ	$= 3.95 \times 10^5$ J kg^{-1}
K_l	$= 100.8$ W m^{-1} K^{-1}
K_s	$= 180.6$ W m^{-1} K^{-1}
ρ	$= 2700.0$ kg m^{-3}
C_{ps}	$= 924$ J kg^{-1} K^{-1}
C_{pl}	$= 882$ J kg^{-1} K^{-1}
μ	$= 10^{-3}$ kg m^{-1} s^{-1}
$d\sigma/dT$	$= -0.35 \times 10^{-3}$ kg s^{-1} °C^{-1}
Process parameters	
r_0	$= 0.5$ mm
R_σ	$= 201\,960.0$
Ma	$= 1851.0$
Ste	$= 1.2117$
Pr	$= 0.009$

Table 2. Numerical and experimental predictions of the melt depth and width after electron beam heating of diameter 1.0 mm

$q \times 10^8$ (W m^{-2})	Width (r^*_{max}/r_0)		Depth (z^*_{max}/r_0)	
	Exp.	Num.	Exp.	Num.
2.43	0.476	0.587	0.292	0.098
3.12	0.820	0.885	0.35	0.260
3.97	0.940	0.988	0.402	0.396
4.10	1.000	1.040	0.460	0.477
5.00	1.154	1.157	0.528	0.796
5.60	1.200	1.220	1.000	0.906

tromagnetic force may also be of the same order as surface tension for the pool of small dimension.

5.2. *Steady state study*

5.2.1. *Flow pattern and heat transfer.* (i) Steel ($r_0 =$ 2.0 mm, $Ste = 3.2516$, $Pr = 0.078$, $R_\sigma = 23\,040.0$, $Ma = 1806.0$). Figures 3(a)–(c) show the isotherm and streamline plots for $B_f = 28.94$, 43.41 and 54.27. These heating factors correspond to power densities of 4×10^8, 6.0×10^8 and 7.5×10^8 W m^{-2}, respectively. The streamline plots show the existence of two contra-rotating cells, one at the top of the pool, the primary cell (clockwise rotation), and another at the bottom of the pool, the secondary cell (anticlockwise rotation). From the stream function values, it can be seen that the strength of the primary circulation increases as the power of the beam increases. These results can be explained as follows. Since the surface temperature gradient increases with increasing power, the strength of the primary cell increases due to the higher convection generating force, i.e. the surface tension gradient. Consequently, the primary convection, i.e. the heat transfer due to the primary cell, also increases and the pool shape becomes shallower due to enhanced radial heat transfer. With the increase of primary convection, which results in the shallow nature of the pool, the secondary cell decreases in size and strength with increasing power. For steel which is of higher Pr ($=0.078$), the secondary circulation decreases with the increase of the beam power. Recently, Basu and Srinivasan [7] also observed the same phenomenon for steel.

The effect of convection on the total heat transfer can be clearly seen from the isotherm plots (Figs. 3–5). Depending upon the flow pattern the isotherms are distorted from the pure conduction isotherms. The extent of distortion is dependent on the strength of the contra-rotating cells. The primary cell stretches the isotherms away from the line of symmetry while the isotherms move downward near the line of symmetry due to the secondary cells. For the cases of higher beam power, the primary convection is the dominant mode of heat transfer and, as a result, the isotherms are flat in nature.

(ii) Aluminium ($r_0 = 2.0$ mm, $Ste = 1.6732$, $Pr = 0.01$, $R_\sigma = 701\,000.0$, $Ma = 6912.0$). Figures 4(a)–(c) show the isotherm and streamlines for $B_f =$ 20.0, 30.0 and 37.47, which correspond to power densities of 4.0×10^8, 6.0×10^8 and 7.5×10^8 W m^{-2}, respectively. The streamline plots show the existence of two contra-rotating cells, as in the case of steel. The strength of the primary cell increases with the power of the beam, but its size does not follow the same trend. The size of the primary cell increases until $q = 6.0 \times 10^8$ W m^{-2} and decreases after that to occupy a small region at the top of the pool for $q = 7.5 \times 10^8$ W m^{-2}. Similarly the size and the strength of the secondary cell decrease until $q = 6.0 \times 10^8$ W m^{-2} and then increase for higher power. Because of the lower Pr value ($=0.01$) the effect of primary convection is smaller, which allows formation of a deeper pool and thereby secondary cells are of higher size and strength. Because of the low Pr value, primary convection at high power cannot form a shallow pool and the primary cell of high strength induces a strong secondary cell. The secondary cells, in turn, make the pool deeper due to enhanced heat transfer near the line of symmetry. The isotherm plots show a strong influence of the secondary cell on the total heat transfer; the shift of isotherms is considerable near the line of symmetry. Because of the dominant nature of both primary and secondary convections, the distortion of isotherms is more than that for steels.

5.2.2. *Pressure distributions.* Figure 5 shows the isobars in the molten pool for steel with $q = 6.0 \times 10^8$ and 7.5×10^8 W m^{-2}, respectively. The interesting feature of these results is the near uniform pressure field in the steady state molten pool for $q = 6.0 \times 10^8$ W m^{-2} ($B_f = 28.94$). Because of the small domain of the molten pool and no body forces (i.e. buoyancy), the flow is fully controlled by the shear force at the boundary resulting from the surface tension gradient. This results in the uniform pressure field for the lower power case. For $q = 7.5 \times 10^8$ W m^{-2} ($B_f = 54.27$), there is a pressure gradient when the pool size is larger. The pressure field of aluminium with $q = 6.0 \times 10^8$

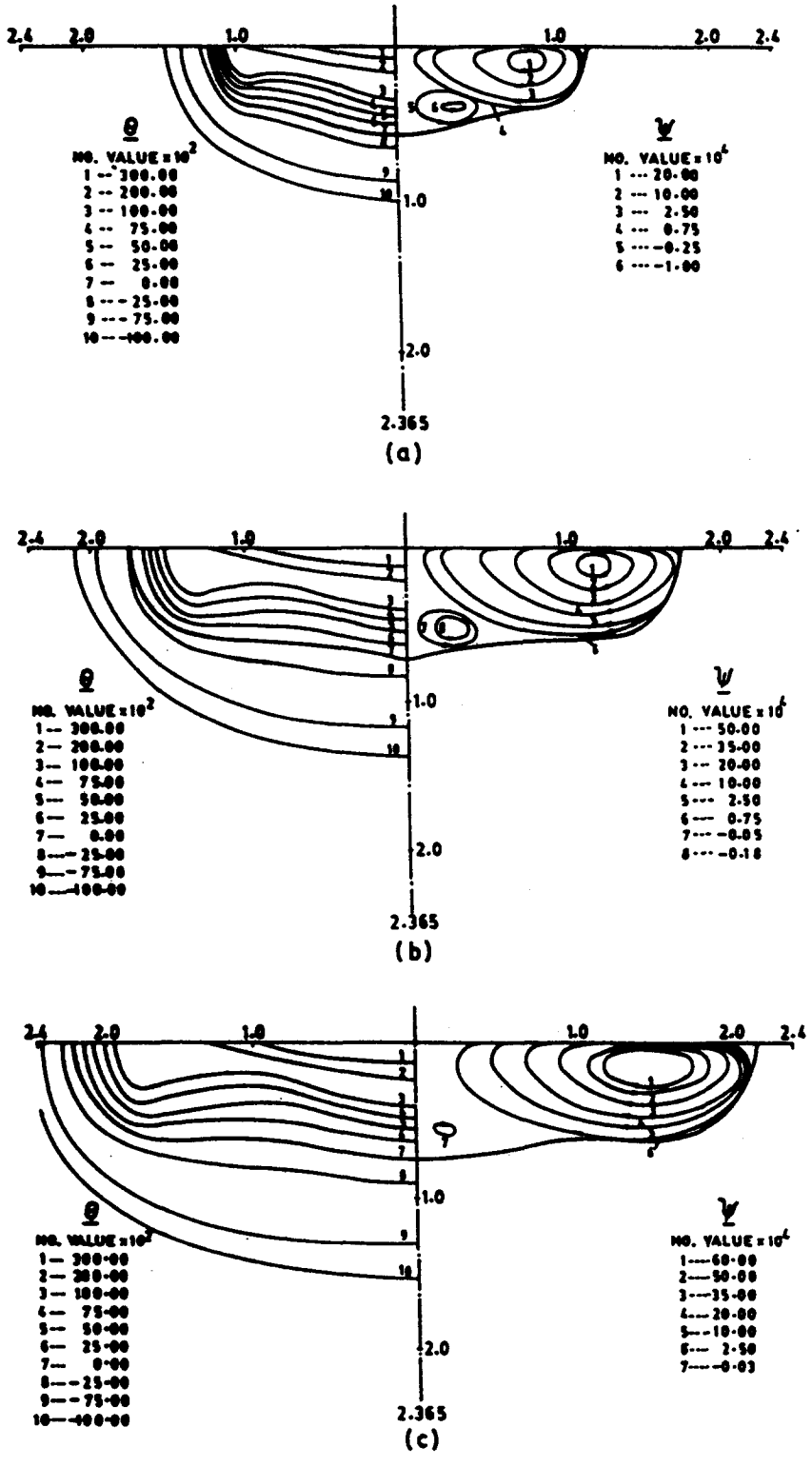

FIG. 3. Isotherm and streamline plots in a steady state molten pool of steel for $B_f = 28.94$ (a), $B_f = 43.41$ (b) and $B_f = 54.27$ (c).

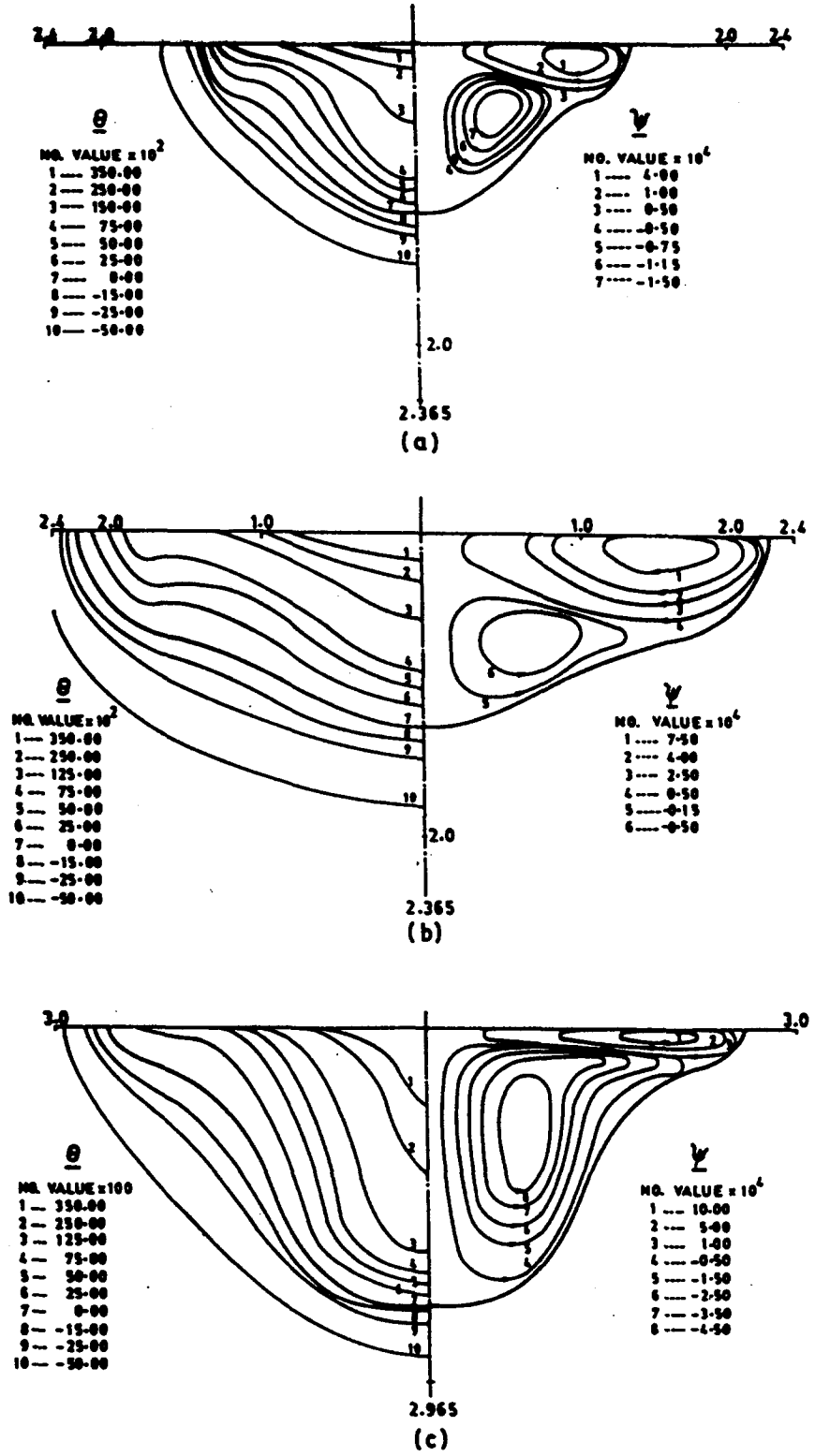

FIG. 4. Isotherm and streamline plots in a steady state molten pool of aluminium for $B_f = 20.0$ (a), $B_f = 30.0$ (b) and $B_f = 37.5$ (c).

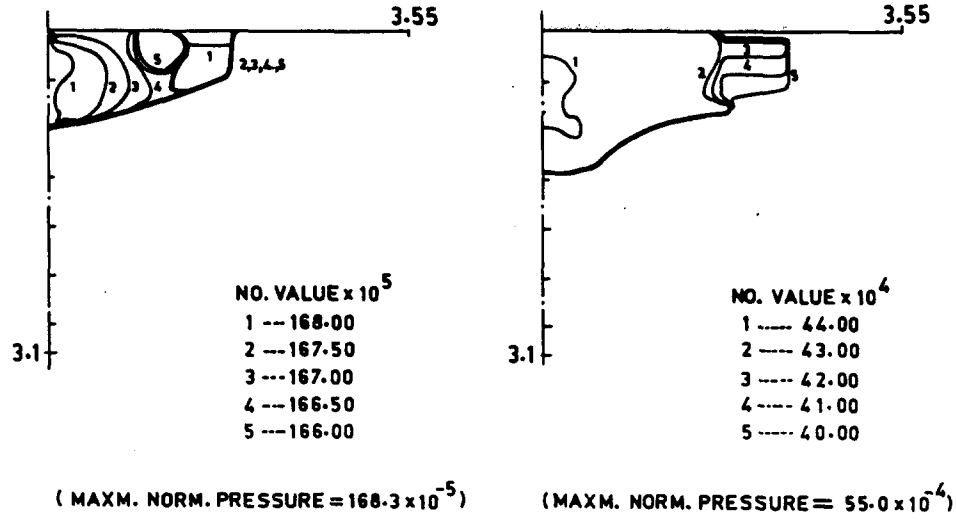

FIG. 5. Isobars in a steady state molten pool for steel with a laser (radius of 2 mm) of power 6.0×10^8 W m^{-2} (a) and 7.5×10^8 W m^{-2} (b).

and 7.5×10^8 W m^{-2} also shows the same trend, i.e. a near uniform pressure field for the lower power case and a nominal pressure gradient for the higher one (see Fig. 6). This result is very important from the point of view of the solution of momentum equations. It may be possible to drop the pressure gradient terms from the momentum equations for certain cases and thereby the solution of momentum equations (in conservative form) will be easier, i.e. no need of staggered grid and pressure correction equation.

5.2.3. *Surface temperature and velocity distribution.* Figures 7(a) and (b) show the surface temperature and velocity distribution for steel and aluminium, respectively. The maximum temperature occurs at the centre of the beam ($r = 0$) and decreases away from the beam. The maximum surface temperature gradient occurs at the edge of the beam ($r = 1$) because of the change in the boundary heat transfer. The surface temperature gradient is therefore higher for beams of higher power. Since the surface tension gradient is the driving force of the fluid flow, the maximum velocity will occur in the region near the edge of the beam, where the maximum temperature gradient exists. This fact can be clearly seen from the surface velocity distributions for all cases. The maximum velocity with a higher powered beam is always higher than that of a lower powered beam because of the higher surface tension gradient. The dimensional values of the maximum velocity for all the cases are as follows.

Steel

$$q = 4.0 \times 10^8 \text{ W m}^{-2}, \quad v_r = 0.51 \text{ m s}^{-1};$$

$$q = 7.5 \times 10^8 \text{ W m}^{-2}, \quad v_r = 0.79 \text{ m s}^{-1}.$$

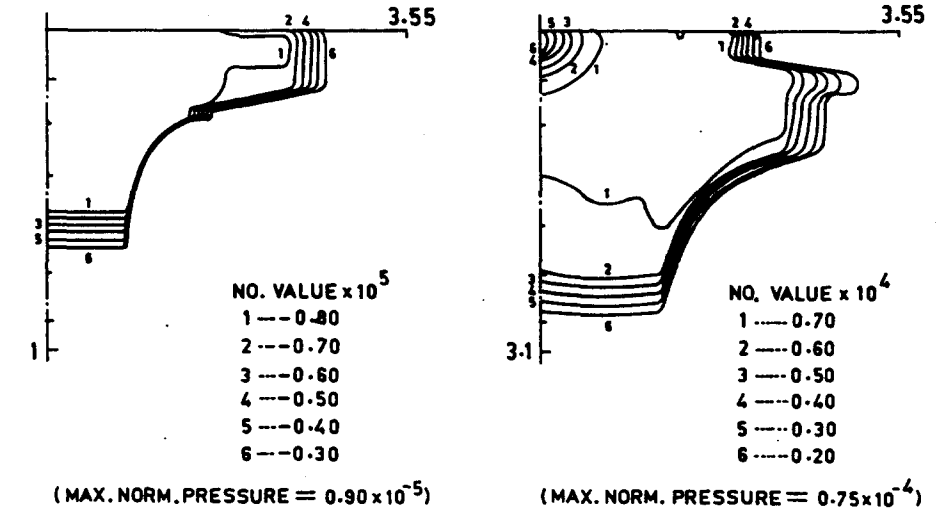

FIG. 6. Isobars in a steady state molten pool for aluminium with a laser (radius of 2 mm) of power 6.0×10^8 W m^{-2} (a) and 7.5×10^8 W m^{-2} (b).

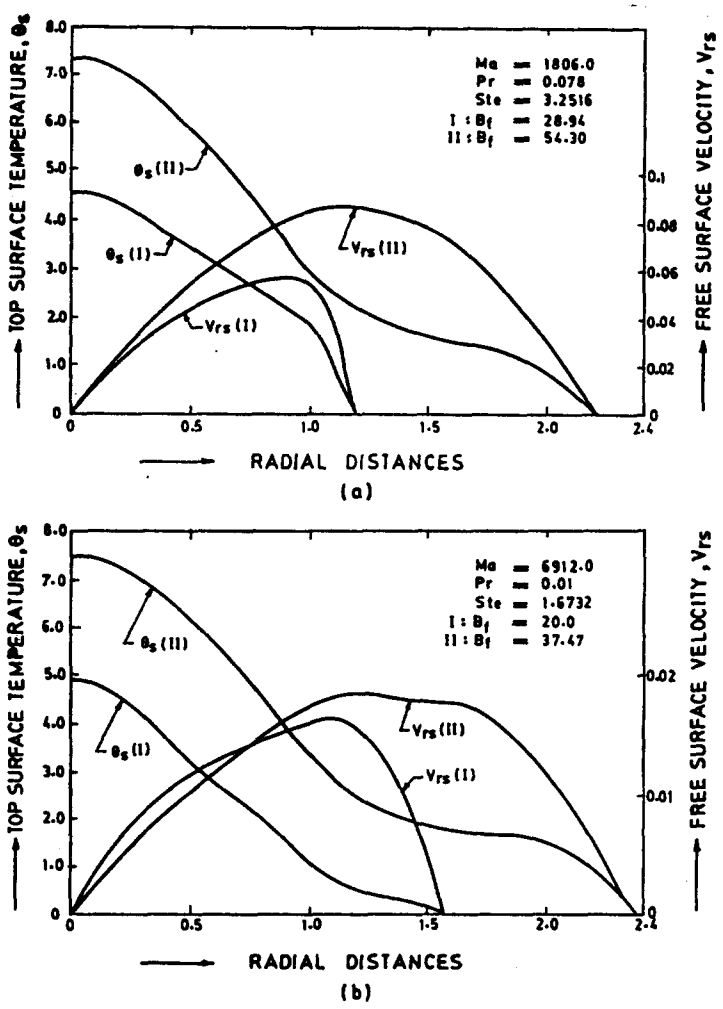

FIG. 7. Top surface temperature and velocity distribution in a steady state molten pool of steel (a) and aluminium (b).

Aluminium

$$q = 4.0 \times 10^8 \text{ W m}^{-2}, \quad v_r = 2.12 \text{ m s}^{-1};$$

$$q = 7.5 \times 10^8 \text{ W m}^{-2}, \quad v_r = 2.42 \text{ m s}^{-1}.$$

The scanning velocity of the laser varies between 0.02 and 0.05 m s^{-1} [5]. Hence, the surface tension velocities in the laser melted pool are considerably higher than the scanning velocity, which results in a negligible effect of the scanning velocity on the flow field, as reported by Chan *et al.* [5] and Srinivasan and Basu [3].

5.3. *Transient study of flow development*

5.3.1. *Steel.* Figures 8(a)–(d) show the transient streamlines for a beam of power 4.0×10^8 W m^{-2} and radius 2.0 mm. Because of the higher *Pr* (=0.078) and *Ste* (=3.2516) values, the primary convection modifies the pool shape faster, i.e. it is shallow in nature, and thereby does not allow the secondary cell to grow.

Interesting results are obtained on the interaction of primary and secondary cells at high beam power, i.e. $q = 7.5 \times 10^8$ W m^{-2}. Figures 9(a)–(f) show the streamlines at different times. The initial development is similar to that of the low power case ($q = 4.0 \times 10^8$ W m^{-2}, Figs. 9(a)–(c)) in size and strength (Figs. 9(c), (d)), and it increases again until time $\tau = 4.8$. The secondary cell shrinks from $\tau = 1.83$ to 2.5 due to the dominant primary convection. In the subsequent times, the interface moves further down near the line of symmetry due to high B_f (i.e. input heat flux) and *Ste* values, and thus allows the secondary cell to grow again. The effect of primary convection is again observed when the secondary cell reduces in size at time $\tau = 6.6$ (Fig. 9(f)). Though the primary cell grows steadily, the growth of the secondary cell fluctuations in nature due to the varying nature of the pool shape resulting from the combined heat transfer processes—conduction, primary convection and secondary convection. Finally, the primary convection dominates and a shallow pool forms at steady state.

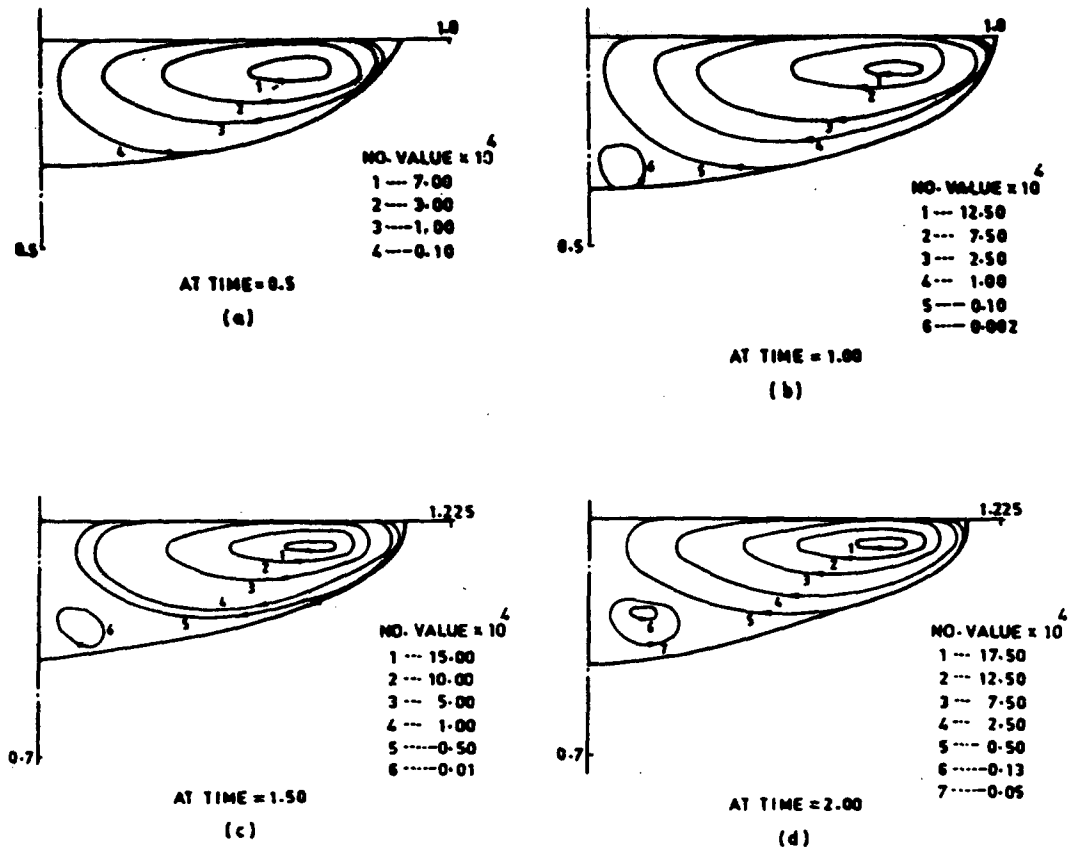

FIG. 8. Transient streamlines and pool shape for steel with $q = 4.0 \times 10^8$ W m^{-2} and $r_0 = 2.0$ mm.

Note that $\tau = 6.6$ corresponds to a near steady state flow distribution (see Fig. 3(c)).

5.3.2. *Aluminium.* Figures 10(a)–(f) show the streamlines at different times with a beam power of 4.0×10^8 W m^{-2} and a radius of 2.0 mm. At small time, i.e. $\tau = 0.09$ (Fig. 10(a)), there is no secondary cell because of the shallow nature of the pool. At $\tau = 0.31$, the secondary cell is already formed (Fig. 10(b)). The flow also develops as can be seen from the maximum value of the stream function. At subsequent times, $\tau = 0.72$ and 1.05 (Figs. 10(c), (d)) and $\tau = 1.45$ and 1.65 (Figs. 10(e), (f)), the secondary cell increases in both size and strength. At $\tau = 1.45$ and 1.65, the secondary cell occupies almost half of the molten pool. The secondary cell forms due to the combined heat transfer and fluid flow during melting: fluid flow controls the heat transfer, heat transfer changes the molten pool and the shape of the pool influences the flow pattern. Primary convection tends to form a shallow pool while the secondary cell makes the pool deeper. The rate at which the shape of the pool changes is dependent on the Stefan number. In the present case of low Pr ($=0.01$) and Ste ($=1.6732$) values, the secondary cell grows due to the inability of primary convection to modify the shape shallow (i.e. low Pr) and quickly (i.e. low Ste).

Figures 11(a)–(e) show the streamlines at different times for a beam power of 7.5×10^8 W m^{-2} and a radius of 2.0 mm. The development of the flow field is similar to that of the low powered beam, i.e. $q = 4.0 \times 10^8$ W m^{-2}. The noticeable difference is the rate of growth of the secondary cell which develops faster. Due to the strong primary circulation and slow rate of change of the pool in the radial direction to form a shallow pool, the secondary cell grows faster. The secondary convection thus increases and the pool shape becomes deeper: Fig. 11(e), which is near steady state, shows a deep pool (see Fig. 4(c)).

6. CONCLUSIONS

The conclusions of this work can be summarized as follows.

(i) The flow field in the laser melted pool consists of two contra-rotating cells: primary and secondary.

(ii) The fluid flow plays an important role on the total heat transfer during laser melting. The distortion of the isotherm from pure conduction isotherms shows the dominance of convective heat transfer.

(iii) The pool shape is shallow in nature for steel while a deeper pool forms for aluminium.

(iv) Under steady state, the secondary cell shrinks with increase in power for steel. For aluminium, the

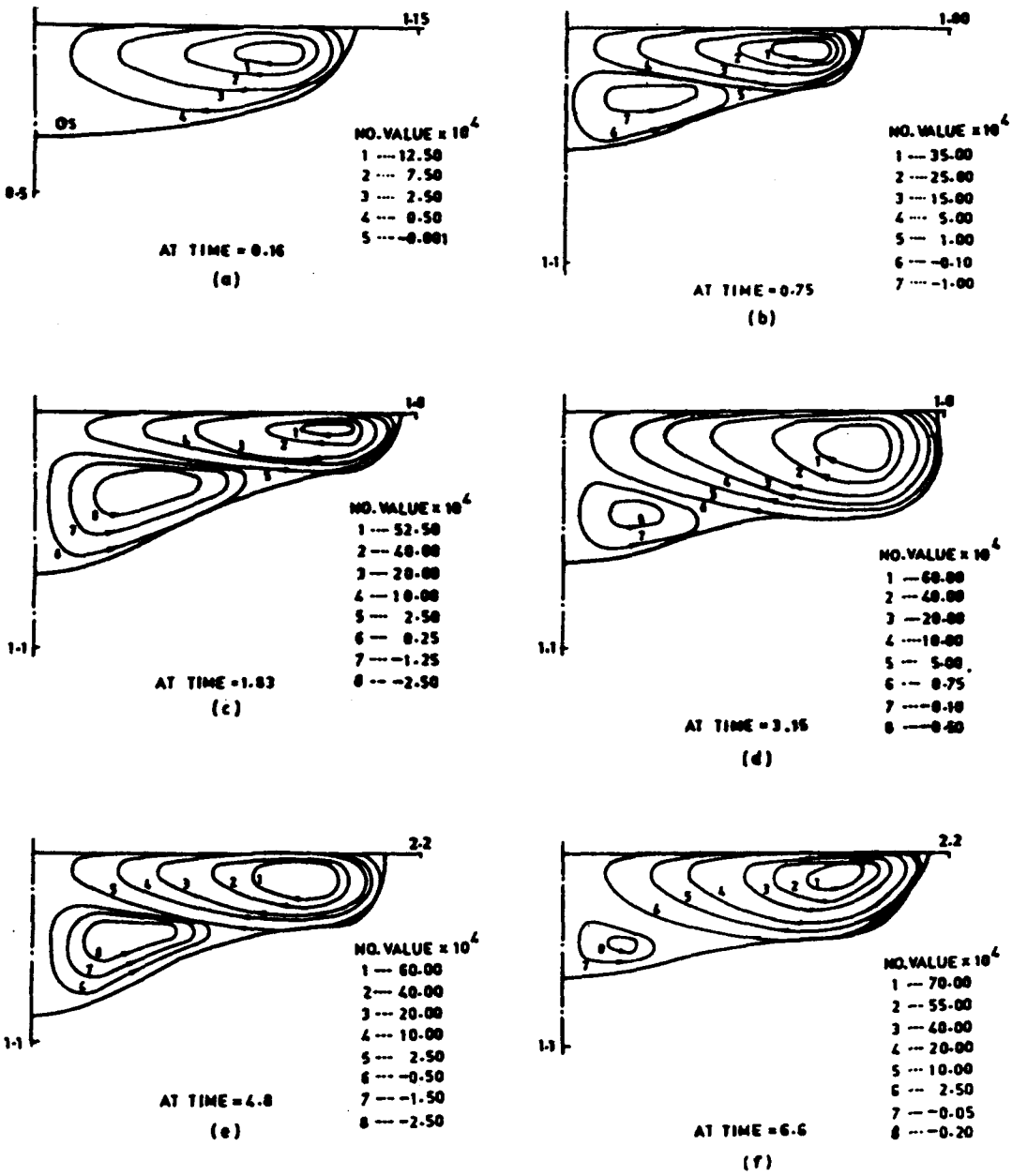

FIG. 9. Transient streamlines and pool shape for steel with $q = 7.5 \times 10^8$ W m^{-2} and $r_0 = 2.0$ mm.

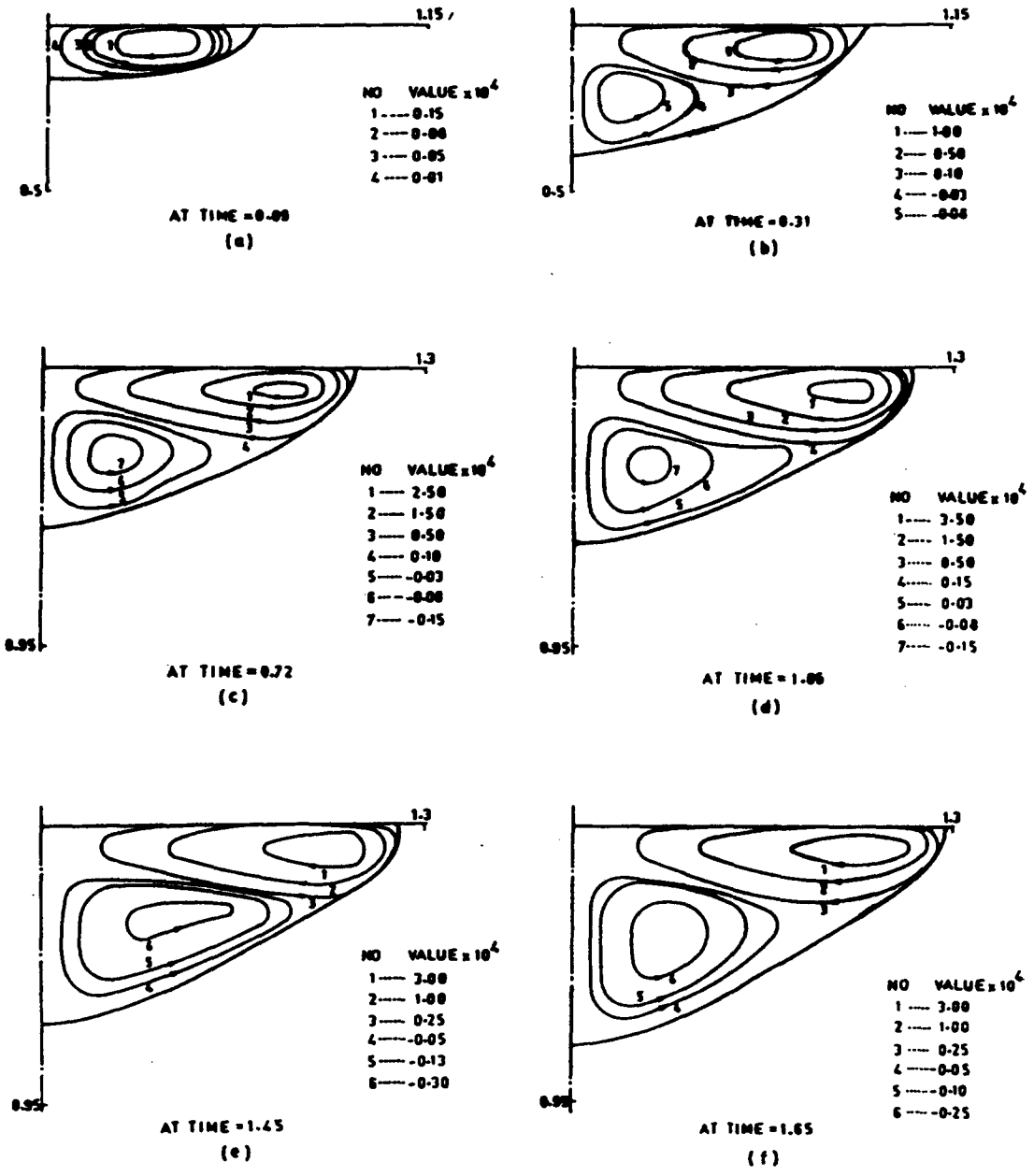

FIG. 10. Transient streamlines and pool shape for aluminium with $q = 4.0 \times 10^8$ W m^{-2} and $r_0 = 2.0$ mm.

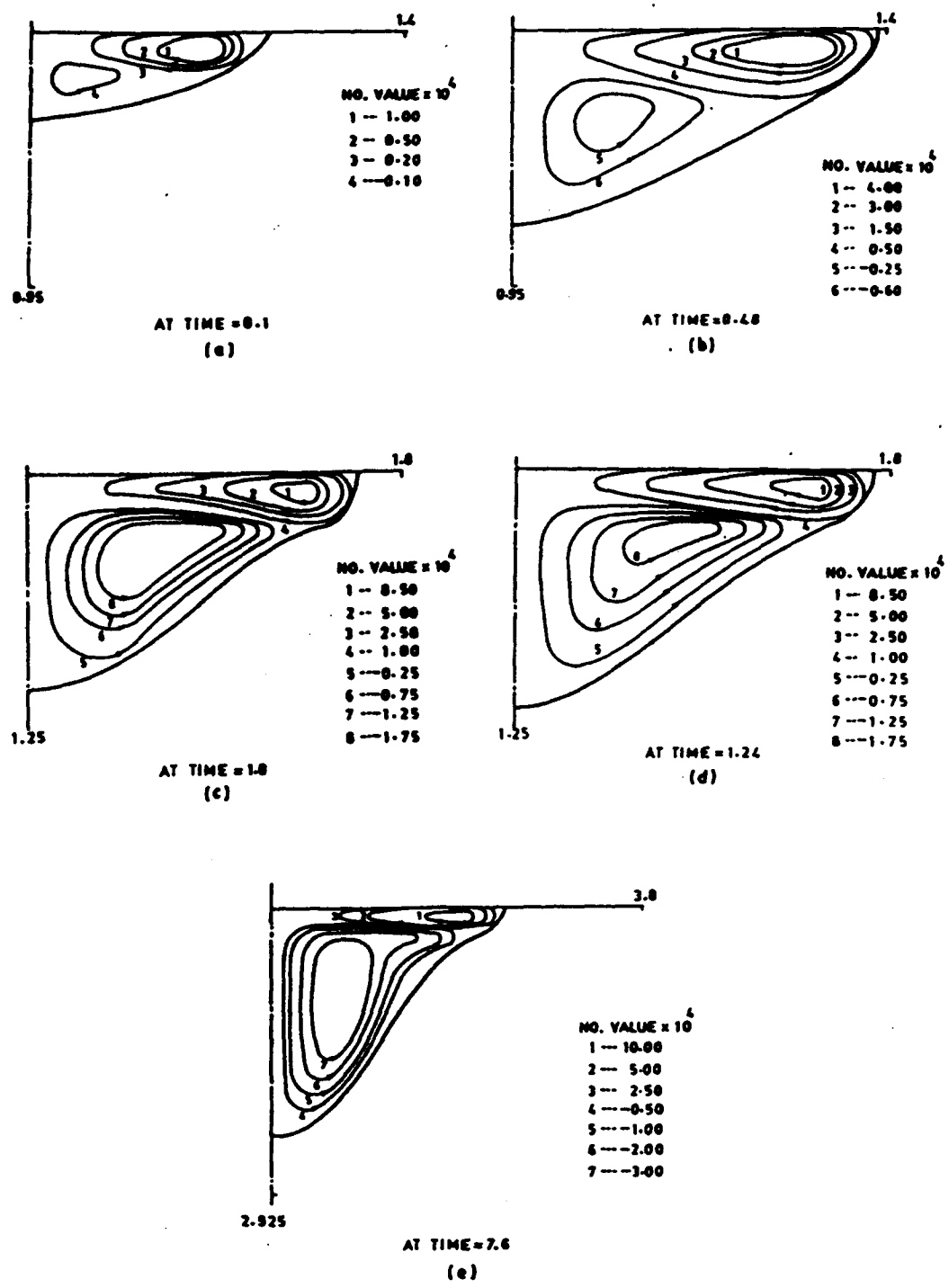

FIG. 11. Transient streamlines and pool shape for aluminium with $q = 7.5 \times 10^8$ W m^{-2} and $r_0 = 2.0$ mm.

secondary cell shrinks until 6.0×10^8 W m^{-2} and increases with further higher power.

(v) The pressure field is uniform for pools of smaller size when $q < 6.0 \times 10^8$ W m^{-2}. This result will be useful in reducing the complexity of the flow calculation, since it may be possible to drop the pressure gradient term from the momentum equation for beams of power lower than 6.0×10^8 W m^{-2}.

(vi) The maximum velocity occurs near the edge of the beam where the surface temperature gradient is maximum. The velocities are found to be considerably greater than the typical scanning velocities.

(vii) The rate of growth of the secondary cell is faster for aluminium than for steel. This is because of the low *Pr* and *Ste* values of aluminium which lead to slower interface movement and a deeper pool.

(viii) The growth of the secondary cell is faster for steel, with a beam power of 7.5×10^8 W m^{-2} and a radius of 2 mm, and fluctuates with time.

Acknowledgements—The authors thank Dr E. C. Subbarao, Director, Tata Research Development and Design Centre, Pune, for many fruitful discussions. This work was supported by a project from the Department of Science and Technology, New Delhi.

REFERENCES

1. R. Mehrabian, S. Kou and A. Munitz, Laser surface melting and subsequent solidification. In *Laser–Solid Interactions and Lasers Processing*. Materials Research Laboratory (1978).
2. T. R. Anthony and H. E. Cline, Surface rippling induced by surface tension gradients during laser surface melting and alloying, *J. Appl. Phys.* **48**, 3888–3894 (1977).
3. J. Srinivasan and B. Basu, A numerical study of thermocapillary flow in a rectangular cavity during laser melting, *Int. J. Heat Mass Transfer* **24**, 563–573 (1986).
4. C. Chan, J. Mazumder and M. M. Chen, Three-dimensional transient model for convection in laser melted pool, *Met. Trans.* **15A**, 2175–2184 (1984).
5. C. Chan, J. Mazumder and M. M. Chen, Three-dimensional model for convection in laser melted pool. Presented at ICALEO-85 (1985).
6. C. Chan, J. Mazumder and M. M. Chen, A model for surface tension flow in laser surface alloying. In *Lasers in Materials Processing* (Edited by E. A. Metzbower), pp. 150–157. American Society of Metals, Metals Park, Ohio (1983).
7. B. Basu and J. Srinivasan, Numerical study of steady state laser melting problem, *Int. J. Heat Mass Transfer* **31**, 2331–2338 (1988).
8. Y. Arata and I. Miyamoto, CO_2 laser absorption properties of metal, Report No. IIW, Doc. IV-50-71, Department of Welding Engineering, Osaka University, Japan (1971).
9. S. V. Patankar, *Numerical Heat Transfer and Fluid Flow* (1st Edn), pp. 120–131. Hemisphere, New York (1980).
10. B. Basu and A. W. Date, On local vs global implicitness during the solution of melting and solidification problems, Paper No. HMT-51-87, *Proc. 9th Natn. Heat Mass Transfer Conf.*, India (1987).
11. J. P. Vandoormal and G. D. Raithby, Enhancement of SIMPLE method for predicting incompressible fluid flow, *Numer. Heat Transfer* **7**, 147–163 (1984).
12. J. A. Sekhar, Rapid solidification of alloy substrates by lasers and electron beams: heat flow modelling and solidification morphology, Ph.D. Thesis, University of Illinois at Urbana-Champaign (1982).
13. S. Kou and D. K. Sun, Fluid flow and weld penetration in stationary arc welds, *Met. Trans.* **16A**, 203–213 (1985).

ETUDE NUMERIQUE DES PROBLEMES PERMANENTS OU VARIABLES DE FUSION LASER—I. CARACTERISTIQUES DU CHAMP D'ECOULEMENT ET DU TRANSFERT THERMIQUE

Résumé—On simule numériquement les problèmes permanents ou variables de fusion laser. On utilise la formulation enthalpique pour résoudre l'équation d'énergie et les équations de quantité de mouvement sont résolues seulement dans le domaine liquide par l'algorithme SIMPLE. A partir d'une distribution gaussienne de flux de chaleur incident, on conduit un large domaine d'étude pour l'acier et l'aluminium en faisant varier la puissance et le rayon du faisceau. La forme du bain et le champ d'écoulement piloté par la tension interfaciale sont complètement différents entre l'acier et l'aluminium. Il existe dans le bain deux cellules contra-rotatives dont la taille et l'intensité dépendent fortement des propriétés du matériau, dont le nombre de Prandtl.

NUMERISCHE UNTERSUCHUNG VON STATIONÄREN UND INSTATIONÄREN LASERGEHEIZTEN SCHMELZVORGÄNGEN—I. STRÖMUNGSFELD UND WÄRMEÜBERGANG

Zusammenfassung—Stationäre und instationäre lasergeheizte Schmelzvorgänge werden numerisch untersucht. Die Energieerhaltungsgleichung wird mit der Enthalpie als abhängiger Variablen gelöst. Die Impulserhaltungsgleichungen werden ausschließlich in der Schmelze mit dem SIMPLE-Algorithmus gelöst. Unter Verwendung einer Gaußverteilung für die aufgeprägte Wärmestromdichte werden eine große Anzahl von Untersuchungen für Stahl und Aluminium durchgeführt, indem Strahlleistungsdichte und Radius variiert werden. Die Formen der Schmelzzone und die durch Oberflächenspannung induzierten Strömungsfelder sind für Stahl und Aluminium recht unterschiedlich. Die Stromlinienbilder zeigen die Existenz zweier gegensinnig rotierender Konvektionszellen in der Schmelze, deren Größe und Stärke ausgeprägt von den Materialeigenschaften, d.h. von der Prandtl-Zahl, abhängen.

ЧИСЛЕННОЕ ИССЛЕДОВАНИЕ СТАЦИОНАРНЫХ И НЕСТАЦИОНАРНЫХ ЗАДАЧ ЛАЗЕРНОЙ ПЛАВКИ—I. ХАРАКТЕРИСТИКИ ПОЛЯ ТЕЧЕНИЯ И ТЕПЛОПЕРЕНОСА

Аннотация—Численно моделируются задачи стационарного и нестационарного лазерного плавления. Для решения уравнения сохранения энергии используется формулировка энтальпии, в то время как уравнения сохранения импульса решаются с применением алгоритма SIMPLE только для гладкой области. На основе Гауссовского распределения подводимого теплового потока приведен ряд исследований для случаев стали и алюминия посредством варьирования плотности мощности луча и его радиуса. Найдено, что форма резервуара и индуцированное поверхностным натяжением поле течения имеют совершенно различный характер для стали и для алюминия. Графики линий тока показывают наличие двух ячеек, вращающихся в противоположных направлениях в объеме расплава, размер и интенсивность вращения которых существенно зависят от свойства материала, т.е. от числа Прандтля.